V. Muscarello, F. Colombo, G. Quaranta, P. Masarati
Aeroelastic Rotorcraft-Pilot Couplings in Tiltrotor Aircraft
Journal of Guidance Control and Dynamics, Vol. 42, N. 3, 2019, p. 524-537
doi:10.2514/1.G003922

Aeroelastic Rotorcraft-Pilot Couplings in Tiltrotor Aircraft

Vincenzo Muscarello*, Francesca Colombo†, Giuseppe Quaranta‡ and Pierangelo Masarati§
Politecnico di Milano, 20156 Milan, Italy

This work investigates rotorcraft-pilot coupling phenomena in tiltrotor aircraft. A detailed tiltrotor model, representative of the Bell XV-15, has been built. Biomechanical models of the pilot, acting on the power lever and on the center stick, are included in feedback loop to define the Pilot-Vehicle System. Pilot-Assisted Oscillation phenomena are investigated on the overall conversion corridor using Nyquist's criterion. Pilot-in-the-loop analyses demonstrate that a critical parameter is detected in the vertical tail geometry. For an asymmetric deflection of the flaperons, the wing's wake impacts on the vertical tail, producing a side force. The pulsating tail-side-force makes the fuselage yaw, and excites the asymmetric wing chord mode coupled with the lateral pilot's biomechanics, leading to a reduction, and in some cases to a loss, of stability. No possibility of unstable events is detected in the longitudinal direction. Conversely, a resonance between the pilot's biomechanics and the aircraft poorly damped symmetric wing bending mode is predicted along the vertical axis. The vertical bounce instability is found along the whole conversion corridor, although the source of excitation changes according to the nacelle angle. Means of prevention are implemented and discussed.

Nomenclature

a_X^{seat} = longitudinal acceleration measured at the pilot's seat, g

a_Y^{seat} = lateral acceleration measured at the pilot's seat, g

a_Z^{seat} = vertical acceleration measured at the pilot's seat, g

G_E = gear ratio between center stick fore/aft displacement and elevator deflection, deg $\cdot$ in.$^{-1}$

G_F = gear ratio between center stick lateral displacement and asymmetric flaperons deflection, deg $\cdot$ in.$^{-1}$

G_T = gear ratio between power-lever displacement and throttle control, deg $\cdot$ in.$^{-1}$

G_0 = gear ratio between power-lever displacement and symmetric collective pitch, deg $\cdot$ in.$^{-1}$

G_{1S} = gear ratio between center stick fore/aft displacement and symmetric longitudinal pitch, deg $\cdot$ in.$^{-1}$

δ_X = fore/aft center stick position, %

*Assistant Professor, Dipartimento di Scienze e Tecnologie Aerospaziali, vincenzo.muscarello@polimi.it.
†M.Sc. Graduate Student, Dipartimento di Scienze e Tecnologie Aerospaziali, francesca9.colombo@mail.polimi.it.
‡Associate Professor, Dipartimento di Scienze e Tecnologie Aerospaziali, giuseppe.quaranta@polimi.it.
§Professor, Dipartimento di Scienze e Tecnologie Aerospaziali, pierangelo.masarati@polimi.it.

δ_Y = lateral center stick position, %

δ_Z = vertical power-lever position, %

δ_P = pedals position, %

ϑ_E = elevator rotation, deg

ϑ_F = asymmetric flaperons rotation, deg

ϑ_T = throttle control, deg

ϑ_0 = symmetric collective pitch, deg

ϑ_{1S} = symmetric longitudinal pitch, deg

μ_p = pilot biomechanical static gain, $\% \cdot g^{-1}$

ζ_p = pilot biomechanical damping ratio, %

ω_p = pilot biomechanical frequency, $\text{rad} \cdot \text{s}^{-1}$

τ_p = pilot biomechanical pole time constant, s

τ_z = pilot biomechanical zero time constant, s

τ = loop transfer function time delay, s

I. Introduction

Adverse interactions between rotorcraft dynamics and human pilot belong to the challenging area of Rotorcraft-Pilot Couplings (RPCs). These phenomena occur when the pilot introduces an inadvertent or unintentional command in the control system as a consequence of the vehicle dynamics, resulting in oscillatory or divergent motion, difficulty in performing the desired task, and, ultimately, loss of control [1]. The interaction between the pilot and the vehicle can be of two kinds. The first one, called Pilot-Induced Oscillations (PIOs), is a sustained or uncontrollable unintentional oscillation resulting from the efforts of the pilot to control the aircraft [2]. Since the human operator's bandwidth is inherently limited, interactions of this nature take place at low frequency, specifically affecting the flight mechanics modes below 1 Hz, see [3]. The second kind of pilot-vehicle interaction is called Pilot-Assisted Oscillations (PAOs), as a result of the unintentional application of controls caused by vibrations of the cockpit. These phenomena involve involuntary pilot participation to the low frequency rotorcraft structural dynamics, usually in the frequency range between 2–8 Hz [3]. Clearly, there is room for overlapping between the two phenomena.

PIO occurrences have been recorded since the very first powered flight attempts by the Wright brothers [4]. A list of PIO events, occurred at civil and military aircraft, is reported by Mitchell and Klyde in [2]. Also rotary-wing aircraft PIOs received some attention throughout the years [5, 6]. A detailed list of events related to rotorcraft is reported in [1], the first known PIO affecting a helicopter, a Firestone XR-9, dating back to 1945 [7]. With reference to tiltrotor aircraft, according to the investigation report [8] a PIO played some role in the accident that occurred to a prototype of the

AW609 civil tiltrotor during flight-testing in 2015. While performing a high-speed descent, the aircraft entered an uncontrolled flying condition due to a series of lateral-directional oscillations. The pilot's roll input was counter phase, although the control laws resulted in an in-phase amplification of the yaw oscillations, making them divergent until each of the proprotors contacted its respective wing, causing structural damage followed by an in-flight break up of the aircraft and subsequent fire. Both test pilots suffered fatal injuries.

A description of PAO instabilities experienced by US Navy rotorcraft is reported by Walden in [9]. Recently, a biomechanical feedback has been recorded on the Bell 525 Relentless, a modern fly-by-wire medium weight helicopter, while flight testing a series of one-engine-inoperative conditions at increasing airspeeds*, resulting in a fatal accident. Tiltrotors too have suffered from several PAO events. Aeroservoelastic pilot-in-the-loop coupling phenomena for the V-22 Osprey are described by Parham et al. in [10]. Three separate instances occurred on the V-22, involving a destabilizing pilot/control device feedback loop which was the main cause of the oscillation. The first was a 1.4 Hz lateral oscillation of the aircraft on the landing gear. The other two PAO events occurred in airplane mode, high speed flight. The antisymmetric wing chord mode was destabilized by the pilot/lateral center stick coupling through the aileron control surfaces at 3.4 Hz. Furthermore, the symmetric wing chord mode was destabilized at 4.2 Hz, as a result of the involuntary pilot's input on the Thrust Command Lever (TCL, i.e. a lever that moves fore/aft) which controls the rotor collective control inputs. In [11], the basic mechanism of the vertical bounce phenomenon in tiltrotors was discussed. This rotorcraft-pilot coupling phenomenon may arise if the pilot's biomechanics interact with the poorly damped symmetric wing bending mode while holding a vertical Power Lever (PL), similar to the collective lever used in conventional helicopters, which is installed on the XV-15 and AW609 tiltrotor aircraft. The vertical displacement of the PL increases the possibility to trigger a PAO phenomenon along the vertical axis. In [11], the phenomenon was investigated only in hover, using a simplified aircraft model characterized by the rigid heave motion and the low frequency out-of-plane wing bending dynamics. Although a simplified model can be extremely useful during an early design stage and to gain insight into the essential aspects of the phenomenon, a detailed aeroservoelastic model of the tiltrotor is often necessary to detect possible RPC phenomena within the overall flight envelope and conversion corridor.

This work presents an effective approach to develop multidisciplinary aeroservoelastic models that can tackle this peculiar type of problems. A detailed tiltrotor model, representative of the Bell XV-15, has been assembled. Section II is dedicated to the description of the dynamic model set-up. The many substructures that are part of the model (airframe structural dynamics, sub-structured nacelles (NACs), unsteady aerodynamics, aeroelastic rotors, servo-actuators, and so on) are outlined. Biomechanical models of the pilot, acting on the power lever and on the center stick, are included in feedback loop to define the Pilot-Vehicle System (PVS). PAO phenomena are investigated on the entire conversion corridor using Nyquist's criterion along the longitudinal, lateral and vertical axes to analyze the stability and the

*https://app.ntsb.gov/pdfgenerator/ReportGeneratorFile.ashx?EventID=20160706X42741&AKey=1&RType=Summary&IType=FA, retrieved on March 28, 2018.

robustness of the PVS (III). Once a possible PAO mechanism is identified, a model reduction is performed to detect the main dynamics and the most influential parameters that can trigger the instability. Finally, means of prevention considering both active-passive devices and cockpit layout modifications are investigated and their pros and cons are discussed. The last section (IV) brings the paper to closure by drawing conclusions about the work performed.

II. Dynamic Model Set-Up

A detailed tiltrotor model, representative of the Bell XV-15 research aircraft with advanced technology blades (ATBs) [12], has been built using the simulation tool MASST (from "Modern Aeroservoelastic State Space Tools"), developed at Politecnico di Milano for the aeroservoelastic and aeromechanical analysis of aircraft and rotorcraft [13, 14]. The dynamic model set-up includes: 1) the airframe structural model, including sub-structured nacelles, 2) airframe unsteady aerodynamics, 3) aeroelastic rotors, 4) a lumped parameter engine drive-train system, 5) servo-actuators, 6) a rotor speed governor controller and 7) pilot/control device biomechanical models. The XV-15 general characteristics are summarized in Table 1. In the following, the many components that are part of the tiltrotor model are described.

Table 1 XV-15 general characteristics.

Characteristic	Symbol	XV-15 (ATBs)	Units
Gross takeoff weight	W_{TO}	13,000	lb
Maximum engine(s) power	P_{max}	2×1,550	hp
Maximum flight speed	V_{max}	280	kt
Wing span	b	32.17	ft
Wing area	S	181.0	ft^2
Rotor radius	R	12.50	ft
Rotor solidity	σ	0.103	n.d.
Rotor Lock number	γ	3.768	n.d.
Rotor rotating speed	Ω	601.0[a]	rpm

[a] Reduced to 80% (480.8 rpm) in airplane mode.

A. Tiltrotor Aeroservoelastic Model

The layout of the Bell XV-15 is similar to a turboprop aircraft. Large proprotors, coupled with turboshaft engines, are mounted on the wingtip nacelles. The rotor axis rotates from the vertical direction, for hover and helicopter mode flight (HEMODE), to the horizontal direction for airplane mode flight (APMODE). According to available literature [15], the airframe structure can be modeled as a finite element (FE) stick model consisting of an elastic wing, which is discretized using 10 beam elements, a rigid fuselage and rigid wing-mounted nacelles. The rotors are represented by two lumped masses. The resulting model is depicted in Fig. 1. It aims at capturing the fundamental six lowest normal modes of the wing, i.e. symmetric/antisymmetric wing bending (SWB/AWB), symmetric/antisymmetric wing chord (SWC/AWC),

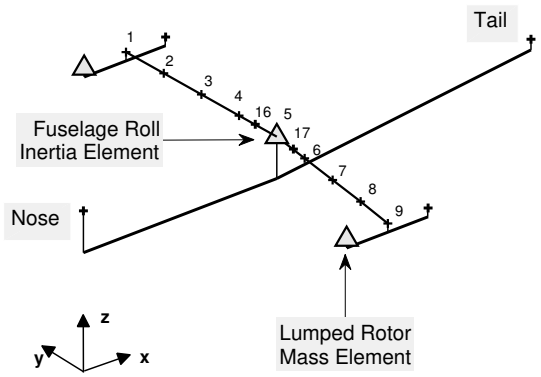

Fig. 1 Bell XV-15 FE stick model.

and symmetric/antisymmetric wing torsion (SWT/AWT). The XV-15 FE stick model describes the tiltrotor structural dynamics in a comparable bandwidth with PAO phenomena (the lowest elastic wing mode is located at 3.3 Hz and the highest at 8.7 Hz) and for this reason it is adopted to represent the elastic airframe, which is developed and validated in NASTRAN. The natural frequencies and mode shapes are validated with the baseline results obtained by Acree et al. [15] in APMODE (see Table 2). Fig. 2 shows the corresponding right rotor hub mode shapes referred to the aircraft body reference frame. The obtained results are considered acceptable.

Table 2 XV-15 airframe natural frequencies (APMODE).

Mode	Frequency, Hz		Difference, %
	NASTRAN	Acree et al. [15]	
SWB	3.20	3.29	-2.74
AWB	6.09	6.27	-2.87
SWC	6.15	6.32	-2.69
AWT	7.48	7.08	+5.65
SWT	8.47	8.34	+1.56
AWC	8.75	8.70	+0.57

One of the main issues with the XV-15 model proposed in Ref. [15] is the rigid connection between the wingtip and the nacelle, referred to as the "downstop-on" configuration. To represent the local compliance between the two substructures, it is decided to replace the clamped constraint with lumped angular springs about the nacelles' pitch and yaw axes. The values assigned to the local springs are initially set to match the APMODE downstop-off frequencies reported by Bilger et al. in Ref. [16], Fig.7. Specifically, the stiffness of the pitch spring is tuned to match the wing torsional frequencies, while the yaw spring stiffness is tuned to match the pylon yaw frequencies. Subsequently, the downstop-off pitch spring is replaced by a three-bar actuator. The nacelle-actuator scheme is depicted in Fig. 3. The

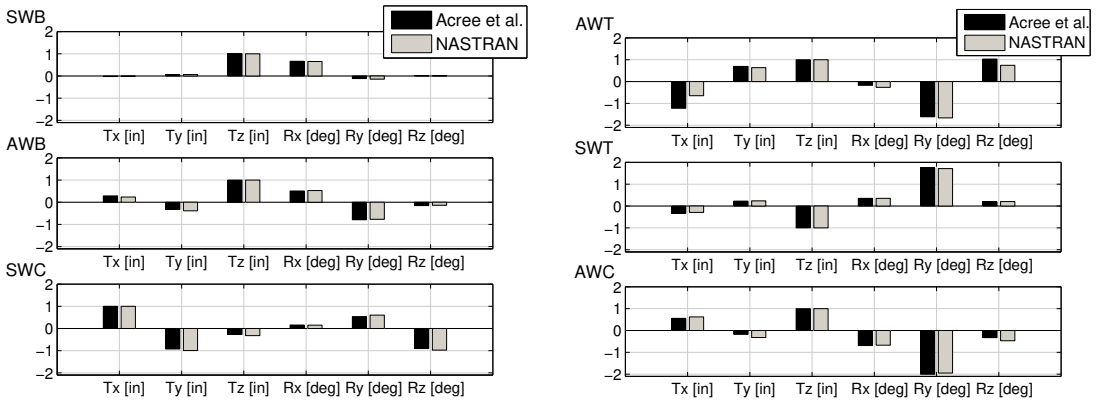

Fig. 2 XV-15 right hub mode shapes (APMODE).

actuator is modeled as a simple rod, whose length changes as a function of the nacelle angle. The equivalent stiffness can be easily evaluated by considering the restoring moment about the spindle axis due to the elastic deformation of the nacelle actuator, namely:

$$M_{(C)} = \frac{EA}{\ell_{AB}} \Delta\ell_{AB} \cdot (\ell_{BC} \cdot cos\phi_n), \tag{1}$$

where: EA is the nacelle actuator axial stiffness, ℓ_{AB} is the variable actuator length, ℓ_{BC} is the distance between the two points BC, $\phi_n = \pi/2 - \alpha_n - \beta_n$, and the elastic deformation $\Delta\ell_{AB} = (\ell_{BC} \cdot cos\phi_n) \cdot \Delta\beta_n$ which yield:

$$K_{ACT} = \frac{EA}{\ell_{AB}} \cdot (\ell_{BC} \cdot cos\phi_n)^2 . \tag{2}$$

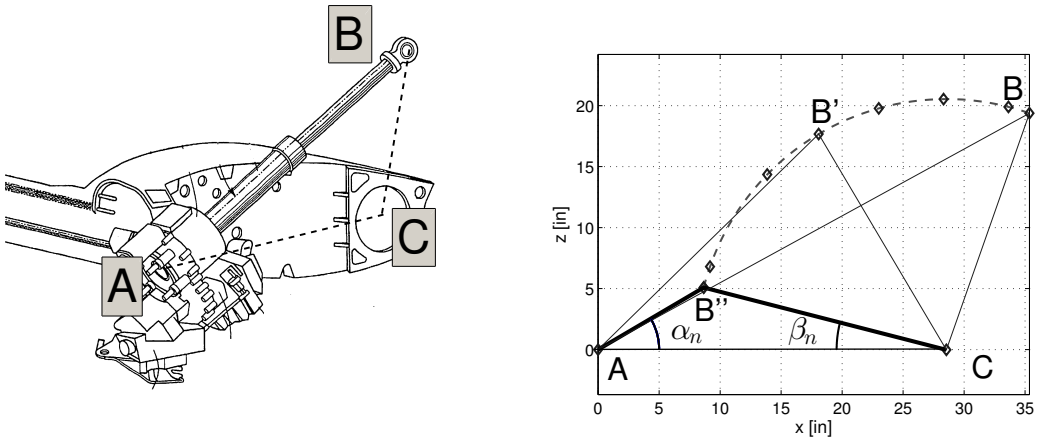

(a) Physical system.

(b) Kinematic model.

Fig. 3 Nacelle-actuator system.

The NASTRAN airframe model is then exported to MASST and divided to three components: the main structure, which includes the wing, the fuselage and the tail, and two substructures that describe the rigid nacelles. In MASST, each nacelle has the specific property to rotate about a spindle axis. As a consequence, a single airframe model can be dealt with for all configurations. The substructuring approach is based on the Boundary Mass Method (BMM) proposed by Karpel and Raveh [17], which requires the user to add large lumped masses (and inertias) to the assembly points, corresponding in the present case to the wing-tip connections, and remove them from the condensed model after reduction. Finally, control surfaces are modeled as well. The XV-15 is supplied with seven aerodynamic control surfaces, namely two flaps, two flaperons, an elevator and two rudders.

Unsteady generalized aerodynamic forces associated with small motion of the airframe and gusts can be obtained as solutions of integro-differential equations related to harmonic boundary domain oscillation, namely the generalized aerodynamic forces frequency responses $\mathbf{f}_a$,

$$\mathbf{f}_a = q_\infty \mathbf{H}_{am}(k, M_\infty)\mathbf{q} + q_\infty \mathbf{H}_{ag}(k, M_\infty)\mathbf{v}_g, \tag{3}$$

where q_∞ is the dynamic pressure, $k = \omega \ell / V_\infty$ is the reduced frequency, M_∞ is the Mach number, $\mathbf{H}_{am}$ and $\mathbf{H}_{ag}$ are the aerodynamic transfer matrices associated with the structural mode shapes $\mathbf{q}$ and the gust input $\mathbf{v}_g$. Matrices $\mathbf{H}_{am}$ and $\mathbf{H}_{ag}$ have been obtained using the classical Doublet Lattice Method (DLM) of NASTRAN [18]. Fig. 4 shows the aerodynamic boxes defined for the XV-15. MASST casts the resulting frequency domain matrices in state-space form by means of a rational approximation reduced to minimum states through a balanced truncation [13, 19].

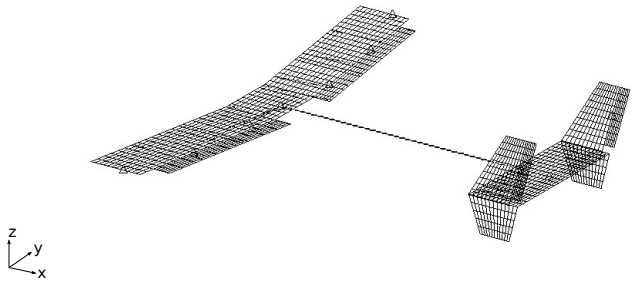

Fig. 4 DLM: XV-15 aerodynamic boxes.

Rotor aeroelastic models are obtained from CAMRAD/JA using data published by Acree in Ref. [20]. Rotor dynamics are generally described by nonlinear differential equations, which can be linearized for a subset of trim configurations representative of the flight conditions of interest (see Fig. 5). Linear time invariant (LTI) models are computed using coefficient averaging to eliminate any periodicity whenever the rotors are not in axial flow conditions. A robust interpolation method is subsequently used in MASST to estimate rotor models for any intermediate trim point (see Ref. [14]). Three bending and two torsion modes, in multi-blade coordinates, plus the rigid lateral and longitudinal

gimbal modes have been considered for the three-bladed, stiff-in-plane, XV-15 rotors. Additionally, each rotor includes: the three-state Pitt-Peters dynamic inflow model [21], the rotor speed degree of freedom and the six hub/pylon rigid modes required to connect the rotor to the airframe, for a total of 27 degrees of freedom. The XV-15 ATBs rotors, which are characterized by composite blades, operate at 601.0 rpm (100%) in helicopter and conversion modes. Once fully converted to airplane mode, the rotor speed is decreased to 480.8 rpm (80%). Table 3 shows the fundamental rotor frequencies in vacuum, for the two rotor speeds. Except for the regressive gimbal and lead-lag modes, all the rotor dynamics are placed above 10 Hz, far away from the PAO frequency range. It must be noted that only the right rotor has been modeled in CAMRAD/JA. The left rotor is obtained in MASST, exploiting symmetry.

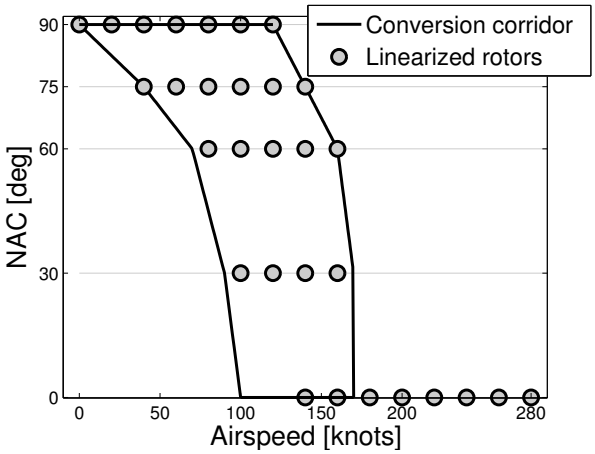

Fig. 5 Linearized rotors on the conversion corridor.

Table 3 XV-15 rotor frequencies in a vacuum.

Mode	HEMODE			APMODE		
	100% rpm, ϑ_0 = 12 deg			80% rpm, ϑ_0 = 40 deg		
	Coll. Hz	Reg. Hz	Prog. Hz	Coll. Hz	Reg. Hz	Prog. Hz
Gimbal	–	0.19	20.22	–	0.24	16.27
1^{st} Bending (Lag)	12.68	3.18	23.22	10.19	2.42	18.45
2^{nd} Bending (Flap)	16.03	17.90	37.93	15.94	22.85	38.88
1^{st} Torsion	30.39	20.85	40.88	28.87	20.44	36.47

Currently, the dynamics of the engine-drive train system can be modeled in MASST using simplified one-dimensional models consisting in a set of torsional springs and equivalent lumped inertias. The XV-15 engine-drive train model is derived from Ref. [22]. In this work, a simplified model is proposed of a symmetric drive train system, shown in Fig. 6. Engines and rotors are approximated as lumped inertias, such as all the components related to the transmission gearings. The reduced parameters I_E, K_E, K_M and the gear ratios, i.e. r_I and r_E, are derived from Ref. [20]. The two gearboxes

are joined by an interconnecting shaft. This system precludes the complete loss of power to either rotor due to a single engine failure, permits power transfer for transient conditions and provides rotational speed synchronization [23]. The long interconnect drive shaft causes the first antisymmetric drive system mode to be in the frequency range of the fundamental wing modes, as shown in Table 4, and thus potentially important for aeroelastic stability.

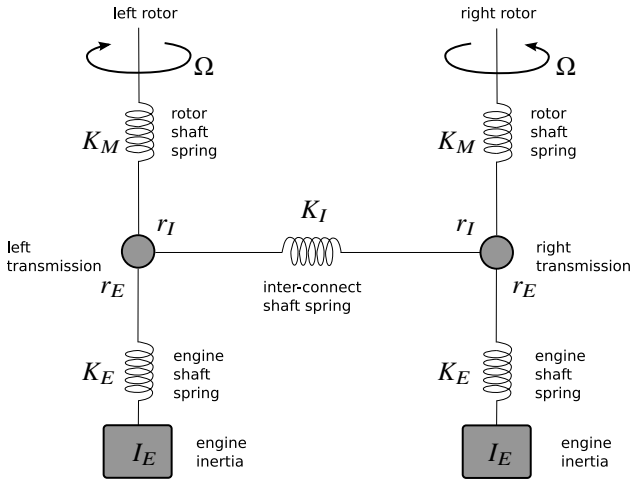

Fig. 6 Symmetric engine-drive train model.

Table 4 XV-15 engine-drive system natural frequencies.

Mode	Frequency, Hz
1^{st} antisymmetric	4.50
1^{st} symmetric	13.98
2^{nd} antisymmetric	16.62

The control surfaces deflection (flaps, flaperons, elevator, rudders) and the rotors pitch inputs (collective and longitudinal cyclic pitch) are actuated by hydromechanical servomechanisms, used for position control. Servo-actuators are represented in MASST by transfer functions that model the servo-valve and compliance dynamics (see Ref. [24], Chapter 9). The motion of a generic control surface, ϑ, is described as a function of the requested motion, ϑ_c, and of the generalized reaction moment applied by the dynamics of the control surface itself, m_c, namely:

$$\vartheta = H_c(s) \cdot \vartheta_c + H_m(s) \cdot m_c, \tag{4}$$

where $H_c(s)$ represents the servo-valve dynamics and $H_m(s)$ is the dynamic compliance. In the XV-15 MASST model, the servo-valve dynamics are described as a second order low-pass Butterworth filter, with a cut-off frequency of 15 Hz. The dynamic compliances of the airframe control surface servo-actuators have been estimated by considering a static stiffness of 200,000 lbf $\cdot$ in $\cdot$ rad^{-1}. The dynamic compliance of the rotor pitch input servo-actuators have been neglected, since their contribution is included in the rotor control chain.

A "Beta" governor is also included. Traditionally, helicopters use throttle governing where the pilot sets the collective pitch and the control system adjusts the engine power to maintain the rpm constant. On the other hand, turboprops generally use "Beta" governing, where the pilot sets the engine power and the governor adjusts the propeller pitch to maintain the rpm constant. For the specific tiltrotor case (see Ref. [23]), a helicopter governing scheme would encounter critical working conditions in APMODE configuration. The torque exhibits high load variations for small collective pitch fluctuations. As a consequence, small pilot's power lever (or thrust command lever) displacements would cause unsustainable torque transients. For this reason, an airplane-like "Beta" governing scheme was chosen during the XV-15 design, which was even considered suitable for the subsequent V-22. The XV-15 "Beta" governor control law, reported in Ref. [20], is characterized by a PI controller that considers as input the error between the requested and the measured rotor rpm. The controller gains (see Tables 17–I and 17–II of Ref. [25]) are scheduled according to the nacelle angle.

B. Pilot's Biodynamic Feedthrough

A general PVS scheme is sketched in Fig. 7. The closed loop system is characterized by a Primary Flight Control System (PFCS), including the gear ratios between the deflection of the control inceptors and the corresponding motion of the control surfaces. The possibility to introduce an Automatic Flight Control System (AFCS), designed to improve the tiltrotor stability and handling qualities, will be investigated in a future work. Pilot-in-the-loop stability analyses are performed by introducing pilot/control device elements in feedback loop with the tiltrotor dynamics. Pilot's biomechanics are generally described by transfer functions that characterize the biodynamic feedthrough (BDFT), i.e. the involuntary control inceptors motion caused by external accelerations transmitted to the pilot's body [26]. Due to the cockpit vibrations the acceleration measured at the pilot's seat, represented as $\mathbf{a}^{seat}$ in Fig. 7, excite the pilot's biodynamics. The output of the pilot's BDFT is an involuntary/passive pilot (PP) input on the control inceptors $\boldsymbol{\delta}^{PP}$. The influence of a voluntary/active pilot (AP) input, $\boldsymbol{\delta}^{AP}$ e.g. due to a pilot model capable of keeping the aircraft in a trimmed condition or to perform a maneuver, is not investigated in this work.

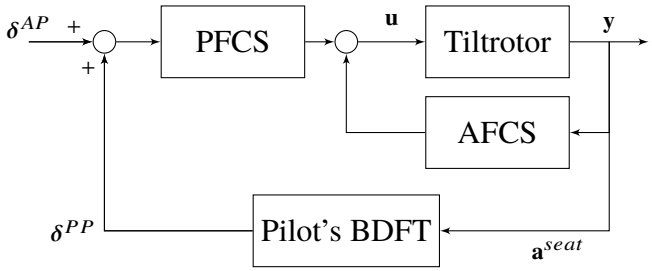

Fig. 7 Tiltrotor Pilot-Vehicle System.

Several pilot BDFTs have been proposed in the literature using data from cockpit mock-up excitation, e.g. Allen et al. [27], Jex and Magdaleno [28] and Höhne [29], flight simulator tests, e.g. Mayo [30] and Masarati et al. [31], and in-flight measurements, e.g. Parham et al. [10]. Zanoni et al. [32] developed a detailed nonlinear multibody

model for the characterization of the upper limbs of human operators, and used it to extract the BDFT. In general, the linearity of the pilot's BDFT for small amplitude oscillations is verified both numerically and experimentally (see Refs. [27, 29, 30, 32–36]).

In MASST the pilot's BDFT is introduced as a controller, since it is actually a control system that takes as input the acceleration measured at the pilot's seat acting on the control inceptors. It is consequently necessary to present the XV-15 cockpit layout. The cockpit controls consist of a center stick, a collective-type power lever (PL) and pedals for the pilot and copilot. Table 5 summarizes the control inceptors excursion.

Table 5 XV-15 control inceptors excursion.

Control Inceptor	Symbol	Min, in.	Max, in.
Fore/aft center stick position	δ_X	−4.8	+4.8
Lateral center stick position	δ_Y	−4.8	+4.8
Vertical power-lever position	δ_Z	0.0	+10.0
Pedals position	δ_P	−2.5	+2.5

A three-position switch on each PL controls the nacelle conversion angle. Pilot controls in HEMODE are similar to those of a conventional helicopter. The PL provides power and collective pitch for heave control, the center stick provides longitudinal/lateral control and pedals are used to control yaw motions. Rolling moments are generated with differential collective, pitching moments with symmetric longitudinal cyclic pitch (fore-aft tip-path-plane rotation) and yawing moments with differential longitudinal cyclic pitch. In APMODE, conventional airplane stick and rudder pedals are employed, whereas the collective stick/power lever remains dedicated to providing power management. The rotor controls are phased out and control moments are generated with standard aerodynamic surfaces: the ailerons generate rolling moments, the elevator generates pitching moments, and the rudders generate yawing moments [37].

Pilot-in-the-loop stability analyses are performed along the longitudinal, lateral and vertical axes. On each axis, the pilot model is defined by a BDFT transfer function (TF). The longitudinal axis pilot BDFT is derived from Ref. [10]. This work presents pilot-in-the-loop aeroelastic analyses of the V-22. The longitudinal pilot's biodynamics is characterized by shaking the pilot in the cockpit with hands on the controls. The pilot's BDFT is identified by measuring the fore/aft stick displacement in response to a longitudinal acceleration. Data available in [38] are used to represent the pilot's BDFT along the lateral axis. In that work, the "Bibby" flight simulator at the University of Liverpool is used as a vibration platform to excite the biodynamics of the pilot along the lateral axis, without any specific visual cueing. Three trained test pilots are considered in the biodynamic feedthrough characterization. Mayo [30] identified a simple model of the BDFT that describes the involuntary action of helicopter pilots on the collective control inceptor when subjected to vertical vibrations. In that case, results were obtained from two sets of pilots, identified as ectomorphic (small and lean build) and mesomorphic (large bone structure and muscle build). As a result, the pilot is modeled as a passive

element that senses a linear acceleration along a single axis and acts over a single control inceptor. In this work, it is speculated that cross-coupling effects, i.e. deflection of all controls other than the mentioned ones as a consequence of excitation along each individual axis, are negligible.

With the presented pilot BDFT transfer functions in the feedback loop with the linearized XV-15 aeroservoelastic models obtained in MASST, only category I Rotocraft-Pilot Couplings can be analyzed [3], i.e. phenomena which do not imply a significant effect of nonlinearities. It cannot be excluded that for large amplitude oscillations the nonlinearities (e.g. actuator saturation, freeplay, deadband, etc...) may have an impact. However, analyzing such effects requires a detailed knowledge of the specific control system of the vehicle, which is outside the scope of the research presented here.

III. Pilot-in-the-Loop Stability Analysis

Including the pilot's BDFT, the PVS is studied by using generalized stability analysis techniques [39]. According to Nyquist's criterion, the degree of stability robustness of a dynamical system can be evaluated by means of two indexes: the gain (G_M) and phase (P_M) margins of the loop transfer function (LTF). In order for a system to be stable, both margins must be positive. The degree of robustness can be quantified by looking at the magnitude of the stability margins. To obtain a robust system it is necessary to reach a gain margin above 6 decibels and a minimum phase margin of 60 degrees, as suggested by Parham et al. in Ref. [40]. Time delays, eventually justified by the digital acquisition and filtering of control device motion or by signal processing before feeding inputs to the actuators [38], can be introduced in the LTF.

A. Instability Mechanism Along the Lateral Axis

Pilot/Lateral Stick Model. This section investigates aeroelastic RPC instabilities involving the tiltrotor lateral dynamics. The analysis is performed in high speed APMODE flight at Sea Level Standard (SLS), ISA[†]+0°C, a flight condition in which large lateral accelerations have already been related to PAO occurrences in the V-22 [10]. In APMODE, a lateral stick motion, δ_Y, generates an asymmetric deflection of the flaperons, ϑ_F. The pilot's control input is managed by the PFCS which contains the gear ratio, $G_F = \partial\vartheta_F/\partial\delta_Y$, between the lateral displacement of the stick and the resulting flaperon rotation. An exponential function representing a time delay τ over the stick control command may need to be accounted for. The gear ratio between the center stick lateral displacement and the flaperon rotation, according to Ref. [25], is equal to G_F = 3.93 deg/in.

The pilot's BDFT is described by the TF reported in Eq. 5. The structural properties identified for the three test pilots in Ref. [38] are reported in Table 6. The complex-conjugate biodynamic poles are well damped, with $\zeta_p > 20\%$. Test pilot 3 shows the highest damping ratio: close to 40%. The natural frequencies ω_p range between 2–3 Hz; pilot 2

[†]International Standard Atmosphere

shows the highest frequency, 2.95 Hz. The static gain, μ_p, of pilot 1 is appreciably higher than that of the other pilots. Moreover, the low natural frequency of the biodynamic pole of this pilot causes a phase reduction at frequencies lower than the other pilots' transfer functions. The different results obtained for pilot 1, compared with the other pilots, are probably related to his anthropometric characteristics: pilot 1 belongs to the 99th percentile in terms of height and weight, showing somewhat different biomechanical properties from those of an average individual.

$$\frac{\delta_Y^{PP}}{a_Y^{seat}} = -\mu_p \frac{s\tau_z + 1}{s\tau_p + 1} \cdot \frac{1}{(s/\omega_p)^2 + 2\zeta_p(s/\omega_p) + 1}. \tag{5}$$

Table 6 Pilot/Lateral stick dynamic properties.

Symbol	Pilot 1	Pilot 2	Pilot 3	Units
μ_p	216.26	88.67	83.88	%/g
τ_z	0.02	0.05	0.03	s
τ_p	0.51	0.49	0.26	s
ζ_p	26.87	23.11	39.66	%
ω_p	13.59	18.53	14.81	rad/s

PAO phenomena in tiltrotor are commonly triggered by a resonance between the pilot's biomechanics and the airframe structural dynamics. As a matter of fact, the lateral PAO reported for the V-22 [10] showed that the pilot's biomechanics, characterized by a biomechanical pole between 2–3 Hz, inadvertently destabilized the AWC mode located at 3.25 Hz. In the XV-15 case, the AWC frequency is located close to 8 Hz (Table 2). Owing to the resulting frequency separation, the possibility for a RPC to occur is unlikely. However, it is recalled that the present XV-15 structural airframe, represented by the FE stick model of Fig. 1, undergoes the strong hypothesis of rigid fuselage. As a consequence, the frequency location of the AWC mode, which involves a consistent participation of the fuselage and tail motion, may be significantly overestimated. With a flexible fuselage, the AWC frequency is expected to reduce. In support of this aspect, many literature sources report that the AWC frequency usually lays within a bandwidth between 3–4 Hz. As an instance, the V-22 AWC frequency was found at 3.25 Hz at 250 knots [10] and the AW609 AWC frequency at 3.76 Hz in vacuum [40]. As a result, it is here decided to artificially modify the XV-15 AWC frequency to a more realistic value of 3.28 Hz.

PAO Analysis. Stability analyses are performed at 280 knots with downstop-on. The time delay is initially neglected. Fig. 8 compares the results obtained with the three test pilot models in feedback loop with the tiltrotor dynamics. The PVS is characterized by robust stability margins.

To further investigate the occurrence of a lateral RPC, it is decided to evaluate the stability margins associated with a potential *High-Gain Pilot*, which is artificially built by retaining all the characteristics of pilot 2, out of the static gain,

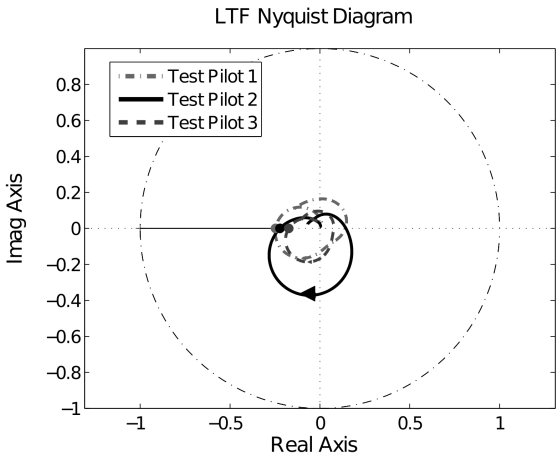

Test Pilot	G_M [dB]	G_M Freq. [Hz]
1	12.16	3.27
2	13.07	3.36
3	15.23	3.31

Fig. 8 Nyquist diagram of the lateral LTF, nominal configuration.

derived from pilot 1. The Nyquist diagram of the LTF, obtained with the *High-Gain Pilot*, is shown in Fig. 9 with black solid line. It can be observed that, despite the sufficiently positive gain margin, the lobe of the Nyquist diagram strongly enlarges with respect to the nominal cases of Fig. 8. The possibility of a PAO phenomenon increases further when a time delay is added on the lateral control device (see Fig. 9). The Nyquist diagram rotates clockwise, thus further reducing the gain margin, which reaches the smallest value for $\tau = 50$ ms.

The plot of Fig. 10 suggests a coupling between the AWC mode and the pilot's lateral biomechanics. The square markers represent the open loop poles (i.e. without the pilot), whereas the poles indicated by the circular markers are obtained with the *High-Gain Pilot* in feedback loop. The pilot's biodynamics decrease the damping of the AWC pole. Increasing the time delay, the AWC pole tends to shift towards the right half of the complex plane, thus losing stability margin. It must be noted that the XV-15 is not known to be prone to lateral PAO phenomena [10]. Coherently, the results presented here show that the eventuality of a lateral PAO is unlikely; considerable losses of stability margins are observed only when the pilot's BDFT is characterized by the envelope of the most unfavorable structural properties of the test pilots. An increase of the pilot's gain and the existence of time delays in the command chain may significantly reduce the stability margins.

PAO Detection. To explain the lateral PAO phenomenon, the effects of the wing's wake vorticity over the XV-15 vertical stabilizers are investigated. Fig. 11 depicts the wing's wake vorticity generated by an asymmetric deflection of the flaperons, inducing a lateral airstream velocity on the two fins. The lateral airstream produces a side force. The pulsating tail-side-force makes the fuselage yaw and excites the asymmetric in plane bending mode, leading to a

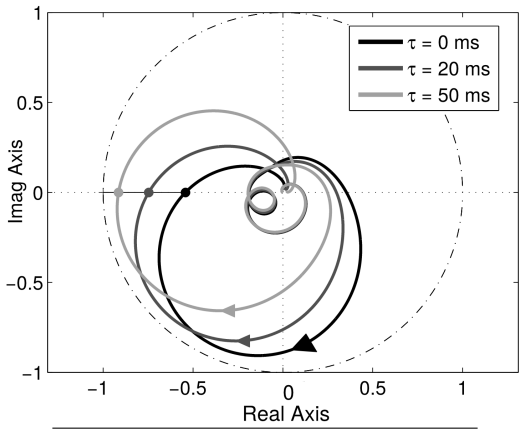

τ [ms]	G_M [dB]	G_M Freq. [Hz]
0	5.33	3.36
20	2.54	3.31
50	0.78	3.27

Fig. 9 Nyquist diagram of the lateral LTF, *High-Gain Pilot*.

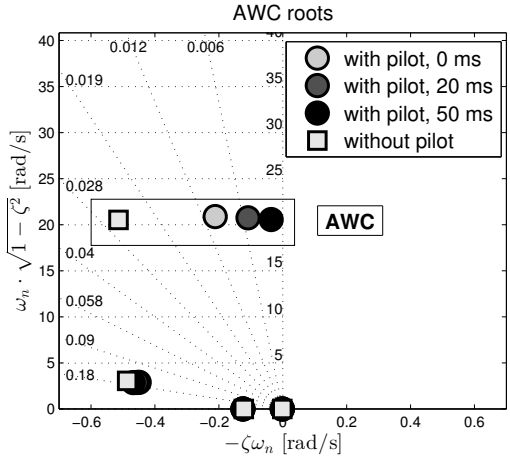

Fig. 10 Evolution of the AWC root with the *High-Gain Pilot*.

reduction, or even a loss, of stability. This aerodynamic interaction is known as *proverse yaw*. The impact of the *proverse yaw* can be quantified by the airframe unsteady aerodynamics included in MASST. The generalized aerodynamic force that energetically works for a rigid yaw rotation, due to an asymmetric deflection of the flaperons, is able to capture this phenomenon. The related aerodynamic TF is indexed as $H_{am}(6, 14)$ (the 6th mode represents the rigid yaw mode and the 14th mode is a rigid, asymmetric rotation of the flaperons). Figure 12 compares the LTFs obtained with and without the aerodynamic TF $H_{am}(6, 14)$. It can be observed that, when this particular aerodynamic contribution is neglected, the lobe in the Nyquist plot contracts considerably, thus increasing the gain margin.

The lateral PAO mechanism can be summarized as follows. The AWC mode induces a lateral acceleration at

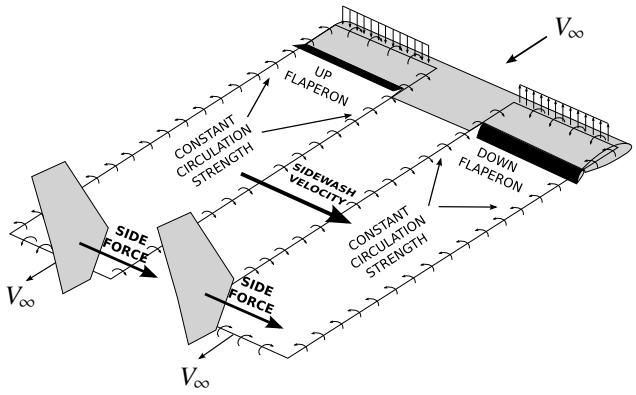

Fig. 11 Flaperon-induced interactional aerodynamic force on vertical stabilizers [10].

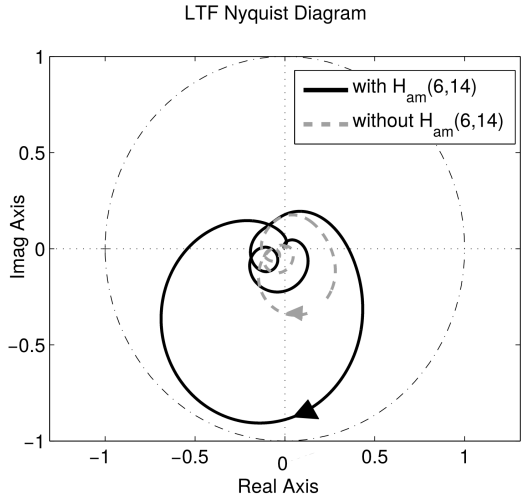

Fig. 12 Nyquist diagram of the lateral LTF with/out the generalized aerodynamic force due to $H_{am}(6, 14)$.

the pilot's seat; this vibration is amplified and delayed by the pilot's biodynamics, producing a lateral displacement of the center stick. The lateral movements of the stick cause the flaperons to rotate asymmetrically, generating a sidewash velocity (and a side force) on the vertical stabilizers and causing the fuselage to yaw. The resulting generalized aerodynamic force excites the AWC mode, closing the feedback loop and producing a destabilizing effect.

Tail Design Modification and Means of Prevention. Consider the flaperon configuration of Fig. 11. The resulting velocity induced by the wing around the vertical stabilizers is depicted in Fig. 13.

In the region above the plane of the wing, the vorticity of the wing generates a sidewash velocity along the positive direction of the y-axis (right semi-wing). On the contrary, in the region below the plane of the wing the velocity field is in the opposite direction. With reference to the configuration shown in Fig. 11, the resulting side force is directed along the positive y-axis. Consequently, in order to potentially magnify the PAO phenomenon, it is decided to modify the original tail configuration by removing the vertical tail surface below the plane of the wing (see Fig. 14(a)).

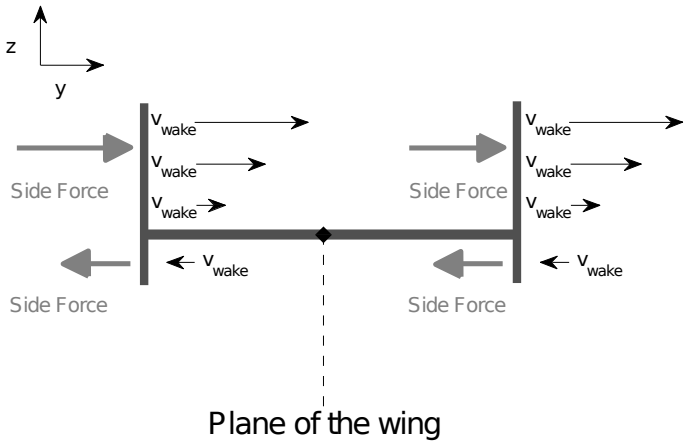

Fig. 13 Induced velocity field around vertical stabilizers.

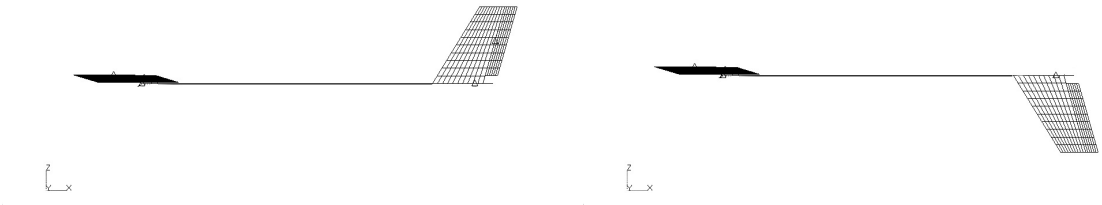

(a) Vertical tail above the plane of the wing.

(b) Vertical tail below the plane of the wing.

Fig. 14 Modified vertical tail geometry.

Pilot-in-the-loop analyses are subsequently performed with the modified vertical stabilizers and test pilot 2. The Nyquist diagram of the LTF is shown in Fig. 15. It can be observed that the lobe of the Nyquist diagram strongly enlarges with respect to the nominal configuration (Fig. 8), thus reducing the stability margins. In addition, time delays in the pilot/control device may consistently further reduce the stability margins of the system.

Similarly, the opposite design modification is investigated, by considering vertical stabilizers located below the plane of the wing, as shown in Fig. 14(b). Based on the previous assumptions, in this region the wing's vorticity produces a sidewash velocity that, colliding with the vertical stabilizers, is supposed to counteract the AWC oscillations. This reversed tail configuration does not actually represent an effective engineering option; one of the main issues is related to the possible violation of ground clearance requirements during take off and landing. However, the considered tail design is only aimed at demonstrating that the proverse yaw can be reduced by moving part of the vertical tail surface below the plane of the wing. The stability of the PVS is examined. Pilot-in-the-Loop analyses are performed with test pilot 2; the influence of possible time delays, introduced by the lateral control device, is initially neglected.

In the plot of Fig. 16, the square markers represent the poles associated with the open loop dynamics, i.e. without the pilot's feedback, whereas the circular markers are associated with the roots obtained with test pilot 2 in feedback

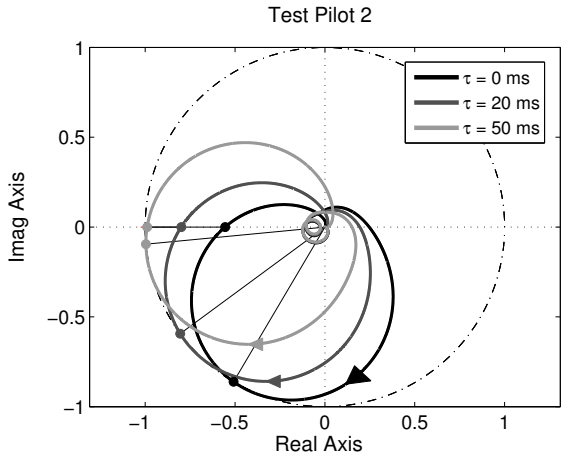

τ [ms]	G_M [dB]	G_M Freq. [Hz]	P_M [deg]	P_M Freq. [Hz]
0	5.11	3.32	59.5	3.25
20	1.96	3.28	36.4	3.24
50	0.09	3.25	5.47	3.24

Fig. 15 Nyquist diagram of the lateral LTF with test pilot 2. Vertical tail above the plane of the wing.

loop. For simplicity, the vertical tail configuration of Fig. 14(a) is, from now on, referred to as *case 1*, while the tail configuration of Fig. 14(b) is referred to as *case 2*. In *case 1* the pilot's BDFT causes the AWC pole to shift towards the right half of the complex plane, thus becoming less stable, while in *case 2* the same pole is moving to the left, becoming more stable.

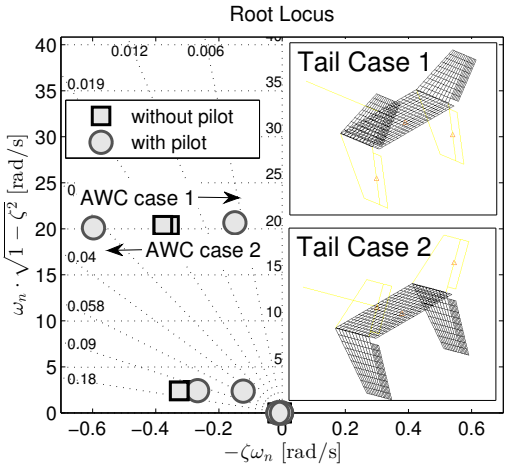

Fig. 16 Comparison between vertical tail configurations.

The Nyquist diagrams of the corresponding LTFs are shown in Fig. 17. The two diagrams are shifted by $\approx 180°$ and the Nyquist plot of *case 2* shows much higher stability margins. The obtained results highlight that the vertical tail design has a non-negligible impact on the lateral PAO mechanism. In this sense, it is recommended to distribute part of the vertical tail surface below the plane of the wing. Results shown in Fig. 8 coherently demonstrate that the nominal

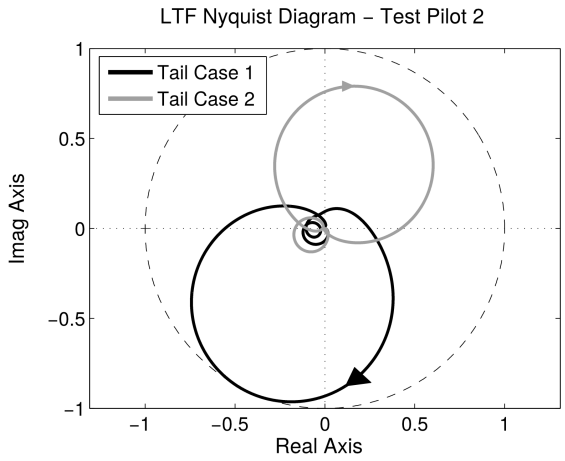

Tail Case	G_M [dB]	G_M Freq. [Hz]	P_M [deg]	P_M Freq. [Hz]
1	5.11	3.32	59.47	3.25
2	19.80	2.78	–	–

Fig. 17 Nyquist diagram of the lateral LTF, comparison between vertical tail configurations.

tail configuration of the XV-15 (Fig. 4) guarantees the PVS stability. As a matter of fact, a large fraction of the area of the vertical stabilizers (30%) is located below the plane of the wing. In the case of the V-22 [10] the area distributed below the plane of the wing was probably insufficient to counteract this specific RPC instability mechanism. It is finally speculated that similar mechanisms may also occur on the AW609, which is characterized by a single vertical stabilizer, entirely located above the plane of the wing.

Other means of prevention may be provided by the implementation of digital structural filters; in Ref. [10], notch filters were included in the PFCS to eliminate the PAO lateral instability. A similar solution will be investigated to suppress vertical PAO phenomena described in the following.

B. Instability Mechanism Along the Longitudinal Axis

Pilot/Longitudinal Stick Model. This section investigates aeroelastic RPC instabilities involving the tiltrotor longitudinal dynamics. In particular, it is intended to analyze the relationship between the involuntary pilot's fore/aft stick control input and the subsequent vehicle motion in the longitudinal direction. On the XV-15 the fore/aft displacement of the center stick, δ_X, generates both a symmetric longitudinal cyclic input, ϑ_{1S}, and an elevator deflection, i.e. ϑ_E. The PFCS includes the gear ratios between the center stick displacement and the control surfaces rotation, namely $G_{1S} = \partial\vartheta_{1S}/\partial\delta_X$ and $G_E = \partial\vartheta_E/\partial\delta_X$. The first one is maximum in HEMODE and decreases with the nacelle angle, becoming null in APMODE (see Table 8a-I, Ref. [25]). The second is constant and equal to $G_E = 4.735$ deg/in [25].

The longitudinal pilot's BDFT is obtained by fitting data obtained by Parham et al. in [10]. The identified TF is

$$\frac{\delta_X^{PP}}{a_X^{seat}} = -\frac{1.808 \cdot 10^4 \cdot s^2 + 2.810 \cdot 10^5 \cdot s + 4.125 \cdot 10^7}{s^4 + 6.491 \cdot 10^1 \cdot s^3 + 2.833 \cdot 10^3 \cdot s^2 + 5.171 \cdot 10^4 \cdot s + 1.050 \cdot 10^6}. \tag{6}$$

In Ref. [10], in order to consider additional pilot variability, the TF data were modified with a higher gain based on twice the measured in-flight pilot's gain. As a result, the data proposed in such reference do not describe the nominal dynamics of a longitudinal pilot/control device but rather a *High-Gain Pilot* TF.

PAO Analysis Pilot-in-the-loop analyses are performed in APMODE and HEMODE flight conditions. In both cases a set of representative airspeeds is considered. Figures 18(a) and 18(b) respectively show the results obtained in APMODE and HEMODE. The Nyquist's criterion indicates stability.

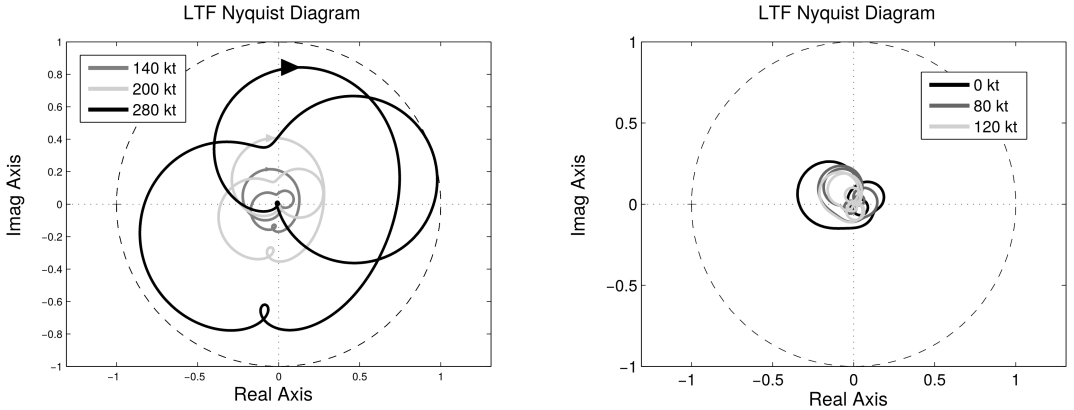

(a) APMODE.

Airspeed [kt]	G_M [dB]	G_M Freq. [Hz]
140	15.68	4.15
200	8.98	4.16
280	1.64	4.16

(b) HEMODE.

Airspeed [kt]	G_M [dB]	G_M Freq. [Hz]
0	9.48	5.33
80	14.70	5.11
120	14.40	5.10

Fig. 18 Nyquist diagrams of the longitudinal LTF.

The small gain margin observed at 280 knots is a consequence of the previously mentioned increased static gain of the pilot. A robust system, with a gain margin of 7.66 dB, is obtained if the nominal pilot's BDFT is considered, which corresponds to halving the gain of the TF used in the analysis. The pilot's biomechanical pole, at 3.95 Hz, is not coupled with any airframe elastic mode and no unstable RPC event is detected along the longitudinal axis. It is worth recalling that in Ref. [10] is described a longitudinal PAO event occurred to the V-22, that destabilized the airframe SWC mode. The unstable oscillations were excited in high speed APMODE flight due to a pulsating thrust induced by the pilot's biodynamics through the TCL, similar to the throttle lever of conventional fixed wing aircraft. In the XV-15, due to the frequency separation between the pilot's biodynamic pole and the SWC mode frequency of the airframe, close to 6

Hz, the possibility for an unstable RPC to occur is unlikely. Moreover, the V-22 TCL is replaced by a power lever on the XV-15, whose vertical motion is not expected to interact with longitudinal accelerations. In summary, thanks to an adequate decoupling between the longitudinal pilot's biodynamics and the airframe symmetric elastic modes, and thanks to the specific cockpit and control inceptors layout, the XV-15 does not appear to be prone to longitudinal PAOs.

C. Instability Mechanism Along the Vertical Axis

Pilot/Vertical Power-Lever Model. In the XV-15 tiltrotor, a vertical power-lever input, δ_Z, acts on the symmetric collective pitch, ϑ_0, and on the throttle control, ϑ_T. The gear ratios are provided by the PFCS: $G_0 = \partial\vartheta_0/\partial\delta_Z$ and $G_T = \partial\vartheta_T/\partial\delta_Z$. The gear ratio between the vertical PL displacement and the symmetric collective pitch is scheduled with the nacelle angle (see Table 8a-IV of Ref. [25]); specifically, the collective input is maximum in HEMODE and null in APMODE. As a consequence, in APMODE the pilot loop closure only takes place by way of the throttle control. The throttle gear ratio is almost constant, with a value of about $G_T = 6.3$ deg/in [25]. The "Beta" governor is also included to maintain constant RPM.

The pilot's BDFT is derived from the work of Mayo [30]. In particular, Mayo identified the TFs between the absolute vertical acceleration of the pilot's hand as a function of the vertical acceleration of the vehicle. As discussed in Ref. [41], these TFs need to be written as the relative acceleration of the hand with respect to the vehicle acceleration and integrated twice to obtain the PL displacement, namely:

$$\frac{\delta_Z^{PP}}{a_Z^{seat}} = -\frac{\mu_p}{s} \cdot \frac{s\tau_z + 1}{(s/\omega_p)^2 + 2\zeta_p(s/\omega_p) + 1}. \tag{7}$$

Table 7 Mayo's TFs structural properties.

Symbol	Ectomorphic	Mesomorphic	Units
μ_p	72.67	64.60	%/g
τ_z	0.117	0.107	s
ζ_p	32.21	28.24	%
ω_p	21.27	23.57	rad/s

It is worth recalling that the double integration gives an integrator-like low-frequency asymptotic behavior, $1/s$, that is not physical (a pilot would always be able to compensate the error corresponding to a slow enough input), and overlaps with the AP behavior. The low-frequency asymptotic behavior can be corrected by adding a second-order high-pass filter with cutoff frequency ω_h slightly above the crossover frequency of the AP model. In this work, a numerical value of $\omega_h = 3.10$ rad/s has been used.

PAO Analysis. A well-known vertical PAO phenomenon is the so-called vertical bounce. It is caused by a pulsating thrust induced symmetrically in both rotors by an involuntary pilot-commanded oscillation of the collective control lever. In helicopters, the reduction of stability margins is rooted in the coupling of the first collective flap (or coning) mode of the main rotor and the biodynamic mode of the pilot's arm holding the collective control inceptor [41]. In classical, stiff-in-plane, gimballed tiltrotors the coning mode frequency is well above the pilot's voluntary/involuntary bandwidth, but the vertical bounce phenomenon may still arise if the pilot's biomechanics interact with the airframe elastic modes, in particular with the SWB mode. Since the XV-15 exhibits a SWB frequency close to 3 Hz (see Table 2), it is here speculated that the pilot's BDFT, showing a resonance in the range between 3–4 Hz (Table 7), may interact with the first airframe symmetric wing mode.

The first stability analyses address the HEMODE configuration with null flight speed, i.e. the hovering condition. Time delays, potentially introduced by the control device, are neglected. The ectomorphic and mesomorphic pilots are included in the PVS. The Nyquist diagrams of Fig. 19 return unstable conditions characterized by marked negative gain and phase margins, as originally predicted by Muscarello and Quaranta in Ref. [11]. The PVS shows that a change in the PL input results in a nearly immediate change in thrust, since at frequencies below that of the coning mode the aeroelastic rotor system responds nearly statically. The thrust change accelerates the tiltrotor vertically, exciting the SWB and, in turn, the pilot's biomechanics. Lower gain and phase margins are obtained with the ectomorphic pilot, since its frequency is closer to that of the SWB mode, and hence to the resonance condition.

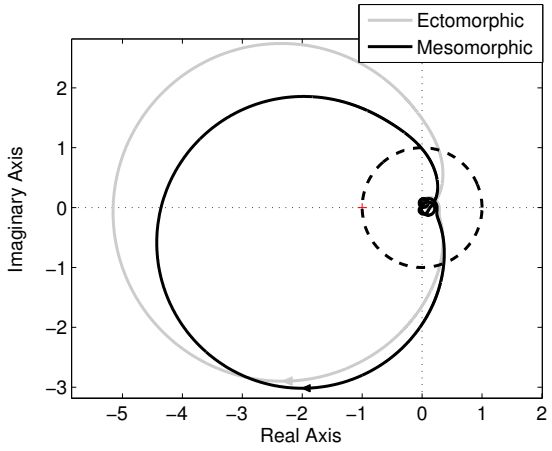

Pilot	G_M [dB]	G_M Freq. [Hz]	P_M [deg]	P_M Freq. [Hz]
Ectomorphic	-14.2	3.01	-106	3.50
Mesomorphic	-12.8	3.04	-89.1	3.51

Fig. 19 Nyquist diagram of the LTF in hover.

The basic mechanism of vertical bounce in tiltrotor aircraft was discussed in [11]. A simplified aeroelastic model, sketched in Fig. 20, was proposed. It is capable of capturing the aircraft heave motion and the low-frequency out-of-plane

wing bending dynamics.

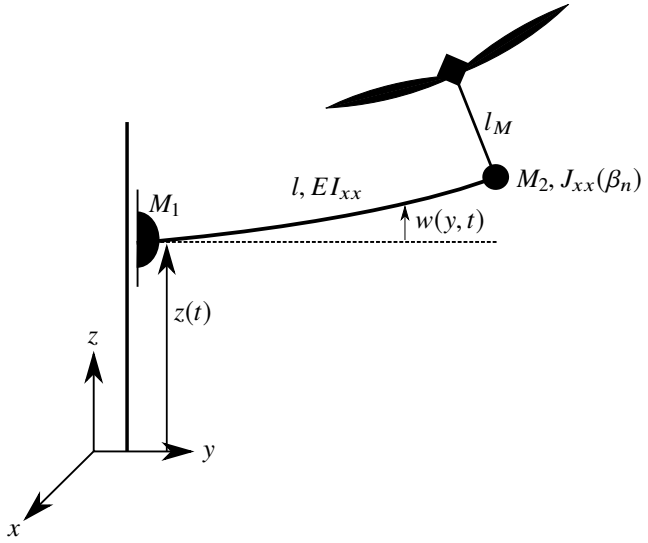

Fig. 20 Simplified 3 DOF model [11].

Results obtained from the simplified model are compared to the ones derived from the more detailed MASST model considered in the present work. The same type of instability is predicted by the two models. The plot of Fig. 21 shows the interaction between the airframe SWB mode and the pilot's BDFT in hover.

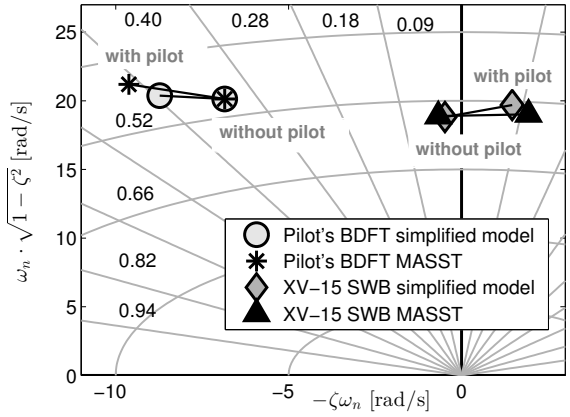

Fig. 21 Eigenvalues in hover, with ectomorphic pilot.

A resonance between the pilot's biomechanical pole and the aircraft poorly damped SWB appears. However, it is worth recalling that the analysis is performed under conservative assumption. The PVS is characterized by several uncertainties: the pilot/control device TFs have been obtained on a flight simulator whose layout differs from that of the XV-15 cockpit, with dissimilar control device dynamics. Moreover, friction in the controls, which is both intrinsic and artificially induced, is not modeled. The absence of friction makes the system more prone to PAOs. The XV-15 was

not affected by pilot biomechanical couplings because it used mechanical control linkages [40]. Anyhow, in modern tiltrotors, mechanical transmission of control input is replaced by a fly-by-wire architecture, that dramatically reduces any undesired friction contribution. Consequently, the presented results may not be fully representative of the XV-15 vertical dynamics, but they can potentially pinpoint issues associated with modern tiltrotor design.

The analysis of the vertical bounce is extended to other flight conditions characteristic of the tiltrotor conversion corridor. A reduced and representative subset of configurations is selected, parameterized with respect to nacelle angle and airspeed. Stability analyses are performed at SLS, ISA+0°C conditions. Since the symmetric collective pitch gear ratio G_0 decreases with the nacelle angle, vertical bounce is expected to disappear when conversion is complete. Moreover, aerodynamic loads in forward flight can potentially magnify the vertical accelerations, thus amplifying the vehicle response to a PL input. As a combined result of these two aspects, the most critical conditions are expected in the region of the conversion corridor that is concurrently characterized by high nacelle angle and large airspeed.

The natural frequencies and the damping ratios of the complex-conjugate SWB poles, obtained as functions of airspeed and NAC angle, are shown in Fig. 22 with the ectomorphic pilot in feedback loop. The vertical bounce frequency ranges from 3 to 3.15 Hz. Greater variability is exhibited by the damping ratio.

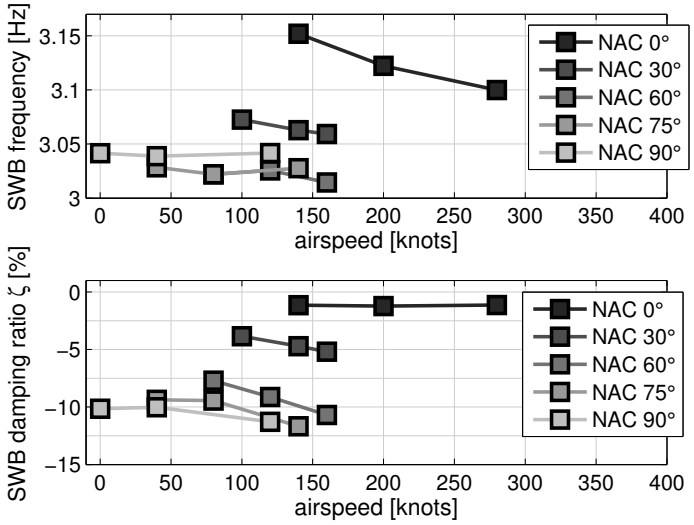

Fig. 22 SWB frequency and damping ratio on the overall conversion corridor, with ectomorphic pilot.

Figure 23 shows the damping ratio contour plots on the conversion corridor, whose analyzed conditions are marked with a circle. As expected, the most critical configurations are detected in the upper region of the conversion corridor. The most critical points correspond to NAC 75-140 kt and NAC 90-120 kt. Again, it can be observed that the ectomorphic pilot generates a more critical instability with respect to the mesomorphic one.

Although the SWB damping ratio becomes less negative when the NAC angle decreases, it can be observed that a mild instability still persists in APMODE. The SWB interacts with the pilot's biodynamic response through a mechanism

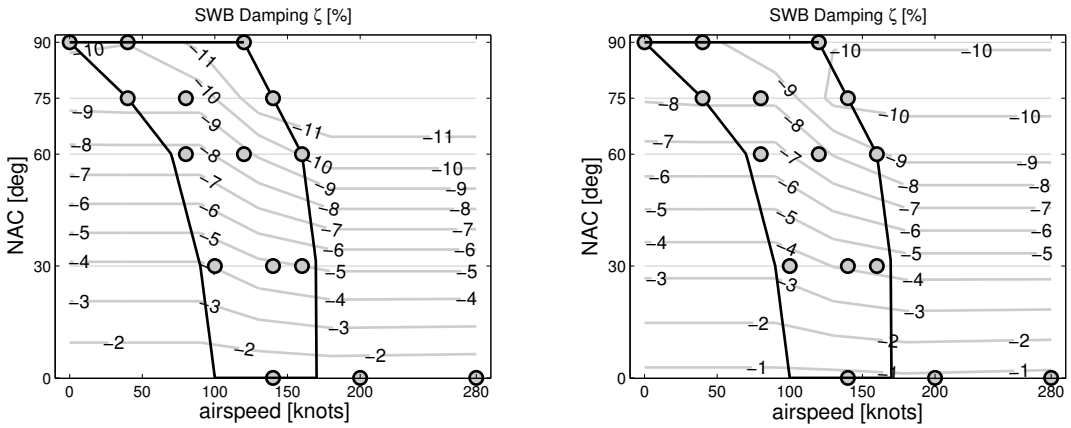

(a) Ectomorphic pilot. (b) Mesomorphic pilot.

Fig. 23 SWB damping ratio on the overall conversion corridor.

that differs from that of HEMODE. Since the thrust vector lays in the plane of the wing, it cannot be held responsible for the excitation of the out-of-plane SWB. The source of the excitation can be traced back to the torque generated by the rotors after a throttle input through the power lever. As depicted in Fig. 24, the wing is supposed to be symmetrically forced by the torque of the counter-rotating rotors.

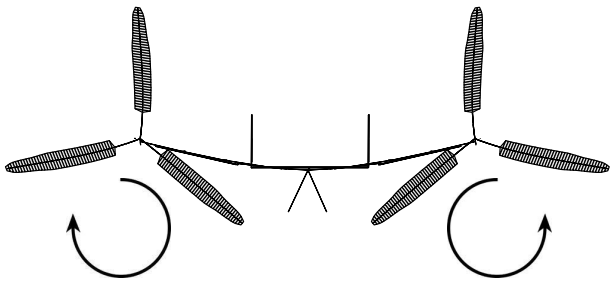

Fig. 24 SWB excitation in APMODE.

Figure 25 compares the SWB damping ratio obtained for three different configurations: 1) the nominal set-up, which takes into account the rotor torque and the pilot's BDFT; 2) a configuration that includes the pilot's BDFT, neglecting the rotor torque transmitted to the airframe; 3) a configuration that includes the rotor torque without the pilot's BDFT (open loop system); confirming that the SWB pole becomes stable when the torque produced by the rotors is not transmitted to the airframe. In general, the torque contribution combines with the pulsating thrust within the conversion corridor, even though the last effect is generally much greater, as discussed in the next paragraph.

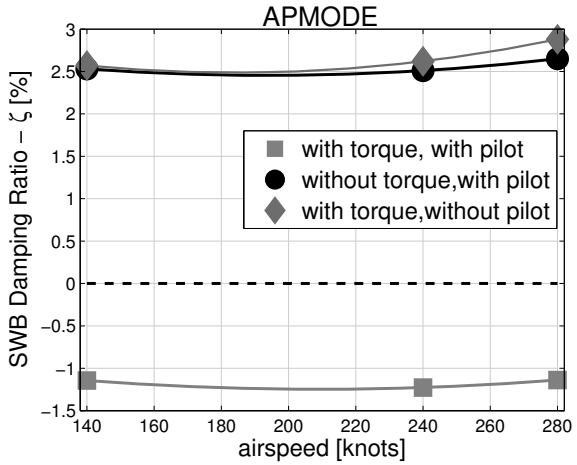

Fig. 25 Torque effect on the SWB damping ratio (APMODE), with ectomorphic pilot.

Effect of Engine – Drive Train – Governor Dynamics. The effect of the engine, drive train and governor assembly — hereafter referred to as EDTG — on the tiltrotor vertical bounce stability is investigated. The EDTG assembly is removed from the XV-15 MASST model and the rotor-speed is assumed constant. The analyses are performed for a subset of representative configurations of the conversion corridor, with the ectomorphic pilot model. Fig. 26 depicts the SWB damping ratio obtained without the EDTG dynamics; no marked difference with the corresponding results of Fig. 23(a) appears in the upper region of the conversion corridor, which remains almost unaltered. The most appreciable effect, instead, can be observed in the lower region of the conversion corridor, especially in APMODE.

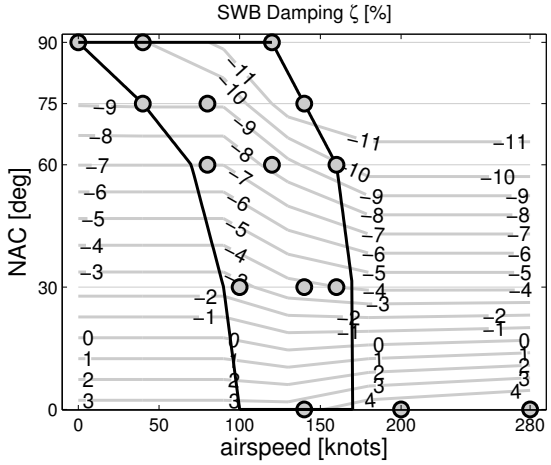

Fig. 26 SWB damping ratio without EDTG dynamics, with ectomorphic pilot.

When the EDTG dynamics are removed, the SWB is stable in APMODE. The engine throttle control is not modeled. Moreover, the collective pitch gear ratio G_0 is null. As a result, both the pilot's inputs are null and the vertical dynamics of the tiltrotor cannot be excited by the pilot's BDFT. These results demonstrate that the EDTG dynamics can be neglected for vertical bounce analyses in HEMODE and in the upper region of the conversion corridor. Conversely, in

APMODE they must be taken into account to correctly reproduce the feedback loop with the pilot's biodynamics.

Means of Prevention. Among the possible means of prevention, the design of a structural notch filter is herein considered, to eliminate the vertical PAO instability. Notch filters (NFs) can suppress the resonance peaks of undesired modes. The structure of a NF, characterized by a second-order TF, is reported in Ref. [11]. Four parameters can be selected for the NF: 1) the notch frequency ω_{NF}, 2) the slope in gain μ (in dB) at the notch frequency, 3) the quality factor Q, where the effects of NFs are significant and 4) the non-dimensional gain value μ_∞ for infinite frequency. The NF is designed to stabilize the SWB pole and to obtain a robust PVS with a gain margin above 6 dB and a minimum phase margin of 60 degrees. A NF attenuates signals within a very narrow band of frequencies; owing to the fact that the SWB frequency only shows very small variations for all the configurations of the conversion corridor (Fig. 22), it is proposed to design a single NF that suppresses vertical bounce in a broad range of flight conditions. The selected NF parameters are reported in Table 8.

Table 8 Notch filter design parameters.

ω_{NF} [Hz]	μ [dB]	Q	μ_∞
2.96	-50	1.32	1

Results are shown in the Bode diagrams of the LTF with and without the NF (Fig. 27), for three configurations. The NF suppresses the instability associated with the most critical scenario. However, it needs be considered that the introduction of the NF in the aircraft FCS produces a phase loss in the LTFs (with NF included) in the low-frequency range, with negative effects on flight dynamics stability. The designed NF introduces a phase delay that ranges from 15 to 20 degrees at 1 Hz, for the flight conditions in the conversion corridor. As a consequence, the impact of the NF on handling qualities must be assessed.

A single NF is able to suppress vertical bounce on the overall conversion corridor, at SLS ISA+0°C conditions and fixed gross weight – CG configuration. The design of scheduled NFs for different configurations can be realized using the simplified 3 DOF model of Ref. [11]. In fact, the simplified analytical model is characterized by lumped parameters and can be easily modified to represent a wide variety of operating conditions and gross weight configurations.

IV. Conclusions

A detailed aeroservoelastic model, representative of the Bell XV-15 tiltrotor research aircraft with advanced technology blades, has been developed to analyze PAO phenomena in tiltrotor aircraft. Lateral pilot-in-the-loop analyses demonstrate that the occurrence of a lateral RPC is an unlikely event when considering the nominal configuration. However, a critical parameter is identified in the vertical tail geometry. In fact, a PAO mechanism can be triggered by the impact of the wing's wake vorticity on the vertical tail produced by asymmetric flaperon deflection. The phenomenon

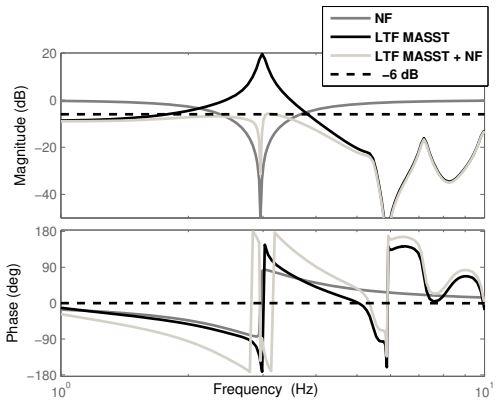

(a) NAC 90 - 120 knots.

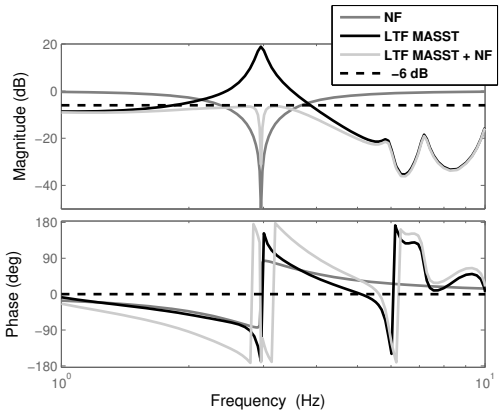

(b) NAC 75 - 140 knots.

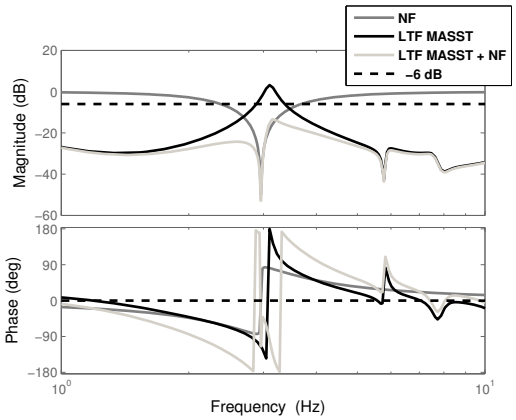

(c) NAC 0 - 280 knots.

Fig. 27 Notch filter on the LTF.

can be exacerbated by a fin design that locates the vertical aerodynamic surfaces above the plane of the wing. It is recommended to distribute part of the vertical tail surface below the plane of the wing, to compensate the destabilizing effect. No unstable RPC is detected in the longitudinal direction. Thanks to an adequate decoupling between the longitudinal pilot's dynamics and the airframe symmetric wing modes and thanks to the specific cockpit configuration, the XV-15 does not appear to be prone to any kind of longitudinal PAO.

Finally, a resonance between the pilot's biomechanical pole and the aircraft poorly damped symmetric wing bending mode is detected along the vertical axis. The most critical configurations are encountered at 75–90 degrees of nacelle angle and maximum airspeed. An airplane mode instability mechanism is also detected, which can be described as a coupling between the symmetric wing bending mode and the pilot's biomechanics due to pulsating symmetric torque, induced by the rotors, through the power lever. It is worth recalling that the analyses are conducted under conservative assumptions, including the absence of friction in the control chain. A notch filter is proposed to suppress the vertical PAOs. The notch filter represents a simple tool to prevent vertical bounce, which can be easily implemented

in aircraft with fly-by-wire systems, although the disadvantages associated with the phase delay in the low frequency range associated with handling qualities must be taken in due account.

References

[1] Pavel, M. D., Jump, M., Dang-Vu, B., Masarati, P., Gennaretti, M., Ionita, A., Zaichik, L., Smaili, H., Quaranta, G., Yilmaz, D., Jones, M., Serafini, J., and Malecki, J., "Adverse Rotorcraft Pilot Couplings — Past, Present and Future Challenges," *Progress in Aerospace Sciences*, Vol. 62, 2013, pp. 1–51. doi: 10.1016/j.paerosci.2013.04.003.

[2] Mitchell, D. G., and Klyde, D. H., "Identifying a Pilot-Induced Oscillation Signature: New Techniques Applied to Old Problems," *Journal of Guidance, Control, and Dynamics*, Vol. 31, No. 1, 2008, pp. 215–224. doi: 10.2514/1.31470.

[3] Dieterich, O., Götz, J., Dang-Vu, B., Haverdings, H., Masarati, P., Pavel, M. D., Jump, M., and Gennaretti, M., "Adverse Rotorcraft-Pilot Coupling: Recent Research Activities in Europe," *Proceedings of the 34th European Rotorcraft Forum*, Royal Aeronautical Society, London, U.K., 2008, pp. 644–692. URL http://hdl.handle.net/20.500.11881/987.

[4] Mitchell, D. G., and Klyde, D. H., "Recommended Practices for Exposing Pilot-Induced Oscillations or Tendencies in the Development Process," *USAF Developmental Test and Evaluation Summit*, American Institute of Aeronautics and Astronautics, Reston, VA, 2004, pp. 1–20. doi: 10.2514/6.2004-6810.

[5] Hamel, P. G., "Rotorcraft-Pilot Coupling — A Critical Issue for Highly Augmented Helicopters?" *AGARD-FVP Symposium on "Advances in Rotorcraft Technology"*, Canada Communication Group, Gatineau, Québec, Canada, 1997, pp. 1–9. URL http://www.dtic.mil/dtic/tr/fulltext/u2/a324206.pdf, Paper 21, AGARD-CP-592.

[6] Ockier, C. J., "Pilot Induced Oscillations in Helicopters — Three Case Studies," Technical Report IB 111-96/12, German Aerospace Center (DLR), Braunschweig, Germany, 1996.

[7] Connor, R. D., "Wrecked Rotors: Understanding Rotorcraft Accidents, 1935-1945," *Proceedings of the American Helicopter Society 66th Annual Forum*, American Helicopter Society International, Fairfax, VA, 2010, pp. 286–312. URL https://vtol.org/store/product/wrecked-rotors-understanding-rotorcraft-accidents-19351945-8419.cfm.

[8] "Accident Occurred to the Agusta Westland AW609 Aircraft Registration Marks N609AG, in Tronzano Vercellese (VC), on the 30th of October, 2015," Aircraft accident report, Agenzia Nazionale per la Sicurezza del Volo, Rome, Italy, October 2015. URL http://www.ansv.it/en/detail_Relazioni.asp?ID=2045.

[9] Walden, R. B., "A Retrospective Survey of Pilot-Structural Coupling Instabilities in Naval Rotorcraft," *Proceedings of the American Helicopter Society 63rd Annual Forum*, American Helicopter Society International, Fairfax, VA, 2007, pp. 1783–1800. URL https://vtol.org/store/product/a-retrospective-survey-of-pilotstructural-coupling-instabilities-in-naval-rotorcraft-3493.cfm.

[10] Parham, T., Jr., Popelka, D., Miller, D. G., and Froebel, A. T., "V-22 Pilot-in-the-Loop Aeroelastic Stability Analysis," *Proceedings of the American Helicopter Society 47th Annual Forum*, American Helicopter Society International, Fairfax, VA,

1991, pp. 1307–1319. URL https://vtol.org/store/product/v22-pilotintheloop-aeroelastic-stability-analysis-906.cfm.

[11] Muscarello, V., and Quaranta, G., "Wing-Pilot Vertical Bounce in Tiltrotors," *Journal of Guidance, Control, and Dynamics*, Vol. 41, No. 8, 2018, pp. 1731–1743. doi: 10.2514/1.G002960.

[12] Maisel, M. D., Giulianetti, D. J., and Dugan, D. C., *The History of the XV-15 Tilt Rotor Research Aircraft: From Concept to Flight*, The NASA History Series, Washington, D.C., 2000, Chap. Flight Research.

[13] Masarati, P., Muscarello, V., and Quaranta, G., "Linearized Aeroservoelastic Analysis of Rotary-Wing Aircraft," *Proceedings of the 36th European Rotorcraft Forum*, Association Aéronautique et Astronautique de France, Paris, France, 2010, pp. 1–10. URL http://hdl.handle.net/20.500.11881/950, Paper 099.

[14] Masarati, P., Muscarello, V., Quaranta, G., Locatelli, A., Mangone, D., Riviello, L., and Viganò, L., "An Integrated Environment for Helicopter Aeroservoelastic Analysis: the Ground Resonance Case," *Proceedings of the 37th European Rotorcraft Forum*, 2011, pp. 1–12. URL http://hdl.handle.net/20.500.11881/835, Paper 177.

[15] Acree, C. W., Jr, Peyran, R. J., and Johnson, W., "Rotor Design for Whirl Flutter: An Examination of Options for Improving Tiltrotor Aeroelastic Stability Margins," *Proceedings of the American Helicopter Society 55th Annual Forum*, American Helicopter Society International, Fairfax, VA, 1999, pp. 997–1012. URL https://vtol.org/store/product/rotor-design-for-whirl-flutter-an-examination-of-options-for-improving-tiltrotor-aeroelastic-stability-margins-4993.cfm.

[16] Bilger, J., Marr, R., and Zahedi, A., "Results of Structural Dynamic Testing of the XV-15 Tilt Rotor Research Aircraft," *Journal of the American Helicopter Society*, Vol. 27, No. 2, 1982, pp. 58–65. doi: 10.4050/JAHS.27.58.

[17] Karpel, M., and Raveh, D., "Fictitious Mass Element in Structural Dynamics," *AIAA Journal*, Vol. 34, No. 3, 1996, pp. 607–613. doi: 10.2514/3.13111.

[18] Albano, E., and Rodden, W. P., "A Doublet-Lattice Method for Calculating Lift Distributions on Oscillating Surfaces in Subsonic Flows," *AIAA Journal*, Vol. 7, No. 2, 1969, pp. 279–285. doi: 10.2514/3.5086.

[19] Roger, K. L., "Airplane Math Modeling Methods for Active Control Design," *AGARD Structural Aspects of Active Controls*, Technical Editing and Production Ltd, London, U.K., 1977, pp. 1–11. URL http://www.dtic.mil/dtic/tr/fulltext/u2/a045242.pdf, Paper 4, AGARD-CP-228.

[20] Acree, C. W., "An Improved CAMRAD Model for Aeroelastic Stability Analysis of the XV-15 with Advanced Technology Blades," Technical Memorandum 4448, NASA Ames Research Center, Mountain View, CA, March 1993. URL https://ntrs.nasa.gov/search.jsp?R=19930013297.

[21] Pitt, D. M., and Peters, D. A., "Theoretical Prediction of Dynamic-Inflow Derivatives," *Vertica*, Vol. 5, No. 1, 1981, pp. 21–34.

[22] Johnson, W., *CAMRAD/JA, A Comprehensive Analytical Model of Rotorcraft Aerodynamics and Dynamics, Johnson Aeronautics Version*, Johnson Aeronautics, Palo Alto, CA, 1988.

[23] Schaeffer, J., Alwang, R., and Joglekar, M., "V-22 Thrust Power Management Control Law Development," *Proceedings of the American Helicopter Society 47th Annual Forum*, American Helicopter Society International, Fairfax, VA, 1991, pp. 1093–1100. URL https://vtol.org/store/product/v22-thrust-power-management-control-law-development-948.cfm.

[24] Merritt, H. E., *Hydraulic Control Systems*, John Wiley & Sons, New York, NY, 1967, Chap. 9.

[25] Ferguson, S. W., "A Mathematical Model for Real Time Flight Simulation of a Generic Tilt-Rotor Aircraft," Contractor Report 166536, NASA Ames Research Center, Mountain View, CA, September 1988. URL https://rotorcraft.arc.nasa.gov/Publications/files/CR-166536_882.pdf.

[26] Quaranta, G., Masarati, P., and Venrooij, J., "Impact of Pilots' Biodynamic Feedthrough on Rotorcraft by Robust Stability," *Journal of Sound and Vibration*, Vol. 332, No. 20, 2013, pp. 4948–4962. doi: 10.1016/j.jsv.2013.04.020.

[27] Allen, R. W., Jex, H. R., and Magdaleno, R. E., "Manual Control Performance and Dynamic Response During Sinusoidal Vibration," Technical Report 73–78, Aerospace Medical Research Laboratory, Wright–Patterson Air Force Base, OH, October 1973. URL http://www.dtic.mil/docs/citations/AD0773844.

[28] Jex, H. R., and Magdaleno, R. E., "Biomechanical Models for Vibration Feedthrough to Hands and Head for a Semisupine Pilot," *Aviation, Space, and Environmental Medicine*, Vol. 49, No. 1–II, 1978, pp. 304–316.

[29] Höhne, G., "Computer Aided Development of Biomechanical Pilot Models," *Aerospace Science and Technology*, Vol. 4, No. 1, 2000, pp. 57–69. doi: 10.1016/S1270-9638(00)00117-6.

[30] Mayo, J. R., "The Involuntary Participation of a Human Pilot in a Helicopter Collective Control Loop," *Proceedings of the 15th European Rotorcraft Forum*, 1989, pp. 1–12. URL http://hdl.handle.net/20.500.11881/2633, Paper 81.

[31] Masarati, P., Quaranta, G., and Jump, M., "Experimental and Numerical Helicopter Pilot Characterization for Aeroelastic Rotorcraft-Pilot Couplings Analysis," *Proceedings of the Institution of Mechanical Engineers, Part G: Journal of Aerospace Engineering*, Vol. 227, No. 1, 2013, pp. 124–140. doi: 10.1177/0954410011427662.

[32] Zanoni, A., Masarati, P., and Quaranta, G., "Rotorcraft Pilot Impedance from Biomechanical Model Based on Inverse Dynamics," *Proceedings of the International Mechanical Engineering Congress & Exposition*, American Society of Mechanical Engineers, New York, NY, 2012, pp. 467–476. doi: 10.1115/IMECE2012-87533, Paper IMECE2012-87533.

[33] Venrooij, J., Abbink, D. A., Mulder, M., van Paassen, M. M., and Mulder, M., "Biodynamic Feedthrough is Task Dependent," *Proceedings of the 2010 IEEE International Conference on Systems Man and Cybernetics (SMC)*, IEEE Publications, Piscataway, NJ, 2010, pp. 2571–2578. doi: 10.1109/ICSMC.2010.5641915.

[34] Venrooij, J., Abbink, D. A., Mulder, M., van Paassen, M. M., and Mulder, M., "A Method to Measure the Relationship Between Biodynamic Feedthrough and Neuromuscular Admittance," *IEEE Transactions on Systems, Man, and Cybernetics, Part B: Cybernetics*, Vol. 41, No. 4, 2011, pp. 1158–1169. doi: 10.1109/TSMCB.2011.2112347.

[35] Zanlucchi, S., Masarati, P., and Quaranta, G., "A Pilot-Control Device Model for Helicopter Sensitivity to Collective Bounce," *Proceedings of the ASME 2014 International Design Engineering Technical Conferences and Computers and Information in Engineering Conference (IDETC/CIE)*, American Society of Mechanical Engineers, New York, NY, 2014, pp. 1–11. doi: 10.1115/DETC2014-34479, Paper DETC2014-34479.

[36] Masarati, P., Quaranta, G., and Zanoni, A., "A Detailed Biomechanical Pilot Model for Multi-Axis Involuntary Rotorcraft-Pilot Couplings," *Proceedings of the 41st European Rotorcraft Forum*, Deutsche Gesellschaft für Luft- und Raumfahrt Lilienthal–Oberth e.V. (DGLR), Bonn, Germany, 2015, pp. 591–601. URL `http://hdl.handle.net/20.500.11881/3621`, Paper 0115.

[37] Maisel, M., "NASA/Army XV-15 Tilt-Rotor Research Aircraft Familiarization Document," Technical Memorandum X-62,407, NASA Ames Research Center, Mountain View, CA, January 1975. URL `https://ntrs.nasa.gov/search.jsp?R=19750016648`.

[38] Muscarello, V., Quaranta, G., Masarati, P., Lu, L., Jones, M., and Jump, M., "Prediction and Simulator Verification of Roll/Lateral Adverse Aeroservoelastic Rotorcraft-Pilot Couplings," *Journal of Guidance, Control, and Dynamics*, Vol. 39, No. 1, 2016, pp. 42–60. doi: 10.2514/1.G001121.

[39] Skogestad, S., and Postlethwaite, I., *Multivariable Feedback Control*, John Wiley & Sons, Chichester, U.K., 2005, Chap. 2.

[40] Parham, T., Jr., and Corso, L. M., "Aeroelastic and Aeroservoelastic Stability of the BA 609," *Proceedings of the 25th European Rotorcraft Forum*, Associazione Italiana di Aeronautica e Astronautica, Rome, Italy, 1999, pp. 1–10. URL `http://hdl.handle.net/20.500.11881/1370`, Paper G3.

[41] Muscarello, V., Quaranta, G., and Masarati, P., "The Role of Rotor Coning in Helicopter Proneness to Collective Bounce," *Aerospace Science and Technology*, Vol. 36, 2014, pp. 103–113. doi: 10.1016/j.ast.2014.04.006.